Int. J. Electrochem. Sci., 15 **(2020)** 7585 – 7600, doi: 10.20964/2020.08.72

International Journal of
ELECTROCHEMICAL
SCIENCE
www.electrochemsci.org

Regulation Polysulfide Conversion by Flexible Carbon Cloth/Molybdenum Selenide to Improve Sulfur Redox Kinetics in Lithium-Sulfur Battery

Hua Yang[1], *Mingshan Wang*[1,*], *Tao Wang*[1], *Hao Xu*[1], *Zhenliang Yang*[2], *Lei Zhang*[2], *Junchen Chen*[1], *Yun Huang*[1], *Xing Li*[1,*]

[1] School of New Energy and Materials, Southwest Petroleum University, Chengdu, Sichuan 610500, P.R. China
[2] Institute of Materials, China Academy of Engineering Physics, Mianyang, Sichuan 621907, P.R. China
[*]E-mail: ustbwangmingshan@163.com (M. Wang); lixing198141@163.com (X. Li)

Received: 5 April 2020 / *Accepted:* 30 May 2020 / *Published:* 10 July 2020

Lithium-sulfur (Li-S) batteries have been regarded as a competitive candidate for next generation electrochemical energy-storage technologies. However, the insulation of charge and discharge products (sulfur and lithium sulfide) and the shuttle efforts of lithium polysulfides (LiPSs), result in not only a series of phase conversion but also sluggish redox kinetics in Li-S electrochemistry. Herein, we firstly designed a flexible carbon cloth/molybdenum selenide (CC/$MoSe_2$) by growing ultra-thin $MoSe_2$ nanosheets on CC as binder-free electrode to understand the regulation mechanism in Li-S battery. With systematic electrochemical investigation of in-situ deposition Li_2S_8 in CC/$MoSe_2$, it is found that CC/$MoSe_2$ exhibits high LiPSs chemical adsorption and electrocatalytic activity, which large enhances the LiPSs conversion. The dynamic regulation of LiPSs change the nucleation and growth of Li_2S, resulting in high uniform distribution on CC/$MoSe_2$ electrode. Thus, it obtains high sulfur redox kinetics and utilization, which achieves initial capacity of 1142 mAh g^{-1} with low capacity fade of only 0.038 % per cycle over 500 cycles at 1 C. Even at high S loading (4 mg cm^{-2}) and extremely low electrolyte/S (E/S) ratio of 6.2 µL mg^{-1}, it still delivers 1204 mAh g^{-1} after 100 cycles at 0.2C with 93.3% capacity maintain.

Keywords: Molybdenum selenide; Binder-free electrode; Lithium sulfide; Lean electrolyte; Lithium-sulfur battery

1. INTRODUCTION

Nowadays, the development of clean energy has attracted extensive attention due to the energy crisis and increasingly serious environmental problems [1, 2]. Excepting for the improvement of energy

conversion technology, the energy storage devices are the key of high efficiency utilization clean energy. Among the various energy storage devices, electrochemical storage devices especially the lithium ion batteries technology have made important progress and being widely used in electrical vehicle, portable electronics, and grid-scale energy storage [3-5]. However, lithium ion batteries based on graphite||lithium cobalt oxides system are facing the limited energy density. It is urgent to exploit more competitive high energy density battery technology to meet the increasing market demands. Among the many candidates, Lithium-sulfur (Li-S) battery is considered as the most potential next generation high energy density battery (2600 Wh kg^{-1}) system, owing to its high theoretical specific capacity of sulfur (1675 mAh g^{-1}), abundant natural resource, low cost and environment friendly [6-11]. Despite of considerable advantages for Li-S battery, it still suffers from some drawbacks that hindering the application of commercialization. Firstly, the insulation of charge and discharge products (S and Li_2S), which results in low electrochemical activity [12-14]. In addition, the shuttle effect of lithium polysulfides (LiPSs) producing from soluble long-chain LiPSs (Li_2S_x, $4 \leq x \leq 8$) back and forth between cathode and anode during the charge and discharge process, leading to decrease of coulomb efficiency and irreversible loss of active materials [15-17]. In response to these issues, increasing the chemical adsorption of LiPSs and synchronous improving the conversion of intermediate LiPSs are the keys to alleviate the migration of LiPSs and strengthen the sulfur redox kinetics.

In the past decades, various approaches have been dedicated to solve the LiPSs shuttle efforts by searching high polar host materials to enhance the chemical adsorption ability of LiPSs on electrode. Amounts of inorganic compounds have been investigated as polar host materials to restrict the LiPSs diffusion by their strong affinity for LiPSs, such as TiO_2 [18], MnO_2 [19], Co_3O_4 [20], FeP [21], Fe_3O_4 [22] etc. However, the problems of sluggish sulfur redox kinetics still not fully understand. Recently, some transition metal dichalcogenides (TMDs) have attracted much attention in energy storage due to their unique two dimensional layers structure, which process abundant edges and unsaturated sites to restrict the diffusion of LiPSs [23-26]. Moreover, those two dimensional materials commonly possess narrow bandgap, usually promoting charge transfer and endowing their catalysis characteristics. As a result, they have already considered as photo-electro-catalysts in the area of solar cells, water splitting and hydrogen evolution [27-31]. Among those TMDs, molybdenum selenide ($MoSe_2$) is typical semiconducting narrow bandgap material, which is consisted of graphene-like Se-Mo-Se layers with van der waals interaction. It contains high surface area along ab plane and abundant active edges, naturally has strong electrocatalytic capability. In addition, some previous researches report that mixed 1H and 2T phase $MoSe_2$ can offer more active sites by the regulation of electronic density at phase junctions, further improving charge transport capacity [32, 33].

On the basis of discussed above, in this work, binder free carbon cloth/$MoSe_2$ (CC/$MoSe_2$) electrode with few-layered mix 1T and 2H phase $MoSe_2$ nanosheets are designed as electrode matrix by in situ growing $MoSe_2$ on CC in Li-S battery. Due to the high electrocatalytic activity from the unique CC/$MoSe_2$ nanostructure, largely accelerates the conversion intermediate LiPSs, further dynamic regulates the nucleation and growth of Li_2S according to utilization Li_2S_8 as active materials. Thus, Li_2S can be uniformly deposited on CC/$MoSe_2$ electrode and maintain high redox kinetics on electrode. The regulation LiPSs conversion mechanism in CC/$MoSe_2$ electrode, combing with the systematic experiment and electrochemical investigation are discussed in details.

2. EXPERIMENTAL SECTION

2.1 Materials

Carbon clothes (CC) were supplied by Shanghai Hesen Electric Co. Ltd. Ketjen black ECP600JD (Lion corporation of japan), $N_2H_4{\cdot}H_2O$ (Chengdu Kelong Co. Ltd., AR, 85%), Ammonium molybdate ($(NH_4)_6Mo_7O_{24}{\cdot}4H_2O$) were purchased from Macklin Biochemical Co. Ltd. Lithium sulfide (Li_2S, AR,99.99%), Sulfur powder (S, AR,99.95%) , and Se power (AR, 99%) were purchased from Aladdin Reagent Co. Ltd. All the chemical reagents were directly used without purification.

2.2 Synthesis of CC/$MoSe_2$

The CC was firstly treated by soaking in acetone under ultra-sonication for 1 h, then further immersing with 1 M HCl solution for 24 h. The pretreated CC was prepared by cutting into round pieces with diameters of 14 mm (1.54 cm^2) after washing with deionized water and drying overnight in 60 ℃ vacuum oven.

The flexible CC/$MoSe_2$ electrodes were synthesized by one step hydrothermal method. Firstly, 0.049 g $(NH_4)_6Mo_7O_{24}{\cdot}4H_2O$ were added in 20 mL deionized water and stirred until completely dissolved. On the other side, 0.0395g of Se powder was added in 5mL of $N_2H_4{\cdot}H_2O$ for stirring 10 min and formation of dark red solution, which is recorded as Se-N_2H_4 solution. Then, the Se-N_2H_4 solution is dropwise added to the configured ammonium molybdate solution with strong stirring. Next, the mix solution was transferred into 50 mL stainless steel Teflon-lined autoclave with adding 4 pieces of CC with the same mass. After fully immersing of CC with 30 min, the autoclave was sealed and put into oven to heat treatment at 200 ^oC for 10 h before cool down to room temperature. Finally, the flexible CC/$MoSe_2$ electrodes were obtained by removal the unreacted solution by washing with deionized water and drying in vacuum at 70 ℃.

2.3 Synthesis *of CC/$MoSe_2$@Li_2S_8*

Firstly, the Li_2S_8 catholyte was prepared by dissolving sulfur and Li_2S (molar ration of 7:1) into 1,3-dioxolane (DOL)/1,2-dimethoxyethane (DME) electrolyte (volume ratio of 1:1) with 2wt% $LiNO_3$ as additives at 80 ℃ in an Ar-filled glove box and obtained 0.01 M Li_2S_8 catholyte standby. Then, the one piece of CC/$MoSe_2$ electrode was soaked into the 1.2 mL of 0.01 M Li_2S_8 catholyte to completely adsorb Li_2S_8 for 12 h until the solution becomes colorless and transparent (with sulfur loading 2 mg cm^{-2}). Then, the electrode with adsorbed Li_2S_8 are taken out and dried for 1 h and prepared to assemble coin cell with Li metal as the counter electrode. The electrolytes are controlled by adding 25 μL 1M LiTFSI in DOL/DME (v/v=1:1) with 0.6 M $LiNO_3$ additive. As a comparison, activated carbon (AC) and sulfur were also mixed by grounding and melting sulfur in AC (the mass ratio of sulfur: AC=4:1) at 155 ℃ for 12 h to obtain AC@S. The AC@S electrodes is prepared by traditional coating technology, which mixing AC@S, Ketjen black, and polyvinylidene fluoride with the mass ratio of 7:2:1 to form uniform slurry. The slurry was coated on Al foil and dried in 60 °C oven for 24 h. The electrode mass was about 3.6 mg

cm^{-2} and the AC@S areal sulfur loading on the disks was 2 mg cm^{-2}. The higher sulfur loading for CC/$MoSe_2$ electrode is prepared by dropping 2.4 mL of 0.01 M Li_2S_8 catholyte (sulfur loading mass is 4 mg cm^{-2}). The ratio of electrolyte/sulfur (μL/mg) are 12.5 and 6.2 for loading sulfur of 2 mg cm^{-2} and 4 mg cm^{-2}, respectively.

2.4 Material characterization

The crystal structure and phase composition of CC and CC/$MoSe_2$ electrode were performed by the X-ray diffraction (XRD, Rigaku D/Max III diffractometer with Cu Ka radiation, 35kV, 60mA). The step scan was performed over the range of 10~80°, with stepping interval of 0.02° and scanning rate of 5.00 deg/min. The composites formation of phase components and structure defective were carried out by Raman spectrometer (Renishaw RM2000, UK) with a 532 nm laser wavelength. The microstructure morphology of those samples were observed by Field-emission scanning electron microscopy (FESEM, JEOLJSM750) and high-resolution transmission electron microscopy (HRTEM, G2F20S-TWIN), respectively. The elemental distributions of composites were investigated by energy dispersive spectrometer (EDS, Oxford, 50 max). The chemical binding of CC/$MoSe_2$ composite and CC/$MoSe_2$/Li_2S_8 electrodes at charge/discharge state were analyzed by using X-ray photoelectron spectroscopy (XPS, PHI 5000 VersaProbe III) equipped with a monochromatic excitation source of Al Ka (1486.68 eV) with X-ray beam size of 100 W power and 20 kV. The pass-energy was set to 280 eV for the survey scans in energy steps of 1 eV. High resolution scans was used a pass energy of 69 eV and step size 0.1 eV. The XPS high resolution unresolved spectra were deconvoluted using XPSPEAK software and fitted based on 20% Lorentz and 80% gauss functions before subtracting the nonlinear Shirley-type background from the spectra. Ultraviolet-visible (UV-vis) absorption spectra were measured to test the adsorption of LiPSs on samples with UV-2550 spectrophotometer (SHIMADZU).

2.5 Electrochemical measurement

The electrochemical performance of self-standing electrode were investigated by assembling CR2032 coin cells in an argon-filled glove box (Dellix industries LTD. (China) LS800S.) with moisture and oxygen levels below 0.1 ppm. The galvanostatic charge-discharge tests were conducted using CR2032 coin cell testing instrument (NEWARE Electronic Co. Ltd, BTS-5 V, 20 mA) from 1.7 V to 2.7 V. Electrochemical impedance spectroscopy (EIS) and cyclic voltammetry (CV) measurements were performed with CHI760E electrochemical workstations. CV was obtained at the scan rate of 0.1 mV s^{-1} with the potential window from 1.7 V to 2.7 V. EIS tests were conducted with sinusoidal excitation voltage applied of 5 mV and frequency range from 100 kHz to 0.01 Hz. Potentiostatic polarization curves were collected with a sweep rate of 0.1 mV s^{-1} at the initial cycle. Tafel plots and corresponding exchange current density values were calculated from potentiostatic polarization curves. The symmetry cells (AC||LiPSs||AC and CC/$MoSe_2$||LiPSs||CC/$MoSe_2$, LiPSs: 0.025M Li_2S_6 in DOL/DME=1:1(v: v)) were assembled and tested through CV scanning at the voltage window of -0.7 to 0.7 V.

3. RESULTS AND DISCUSSION

Figure 1a shows the XRD image of prepared CC/$MoSe_2$ electrode, all the main peaks positions are similar with the 2H $MoSe_2$ (PDF No. 29-0914).

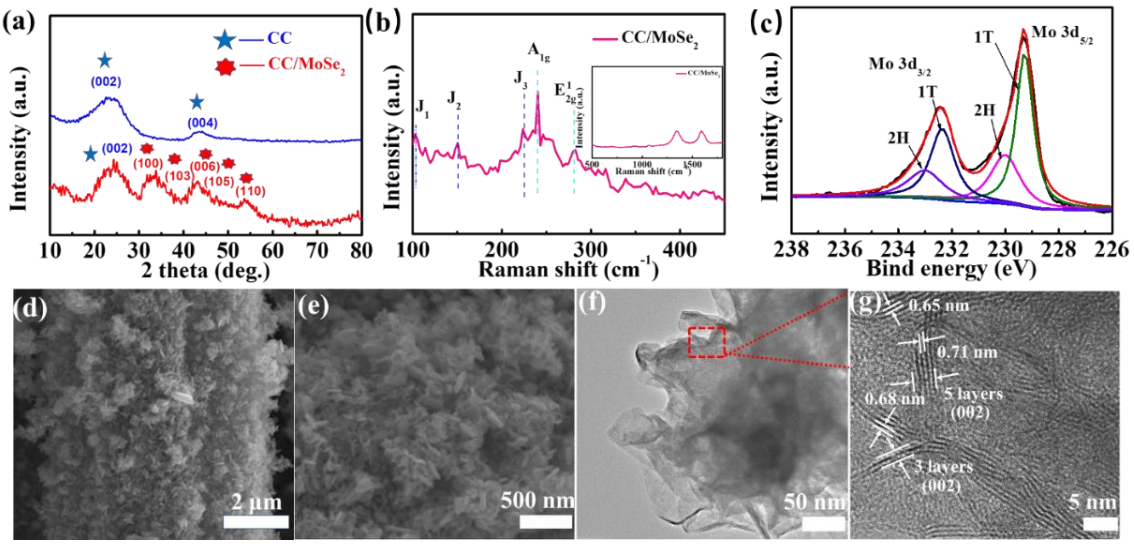

Figure 1. (a) XRD patterns of CC, CC/$MoSe_2$; (b) Raman spectra of CC/$MoSe_2$; (c) XPS spectrum of Mo 3d in the as prepared CC/$MoSe_2$; (d) and (e) FESEM images of CC/$MoSe_2$; (f) and (g) HRTEM image of $MoSe_2$.

However, the (002) peak at 12.5° disappear, which is ascribe to the partly phase conversion of 2H $MoSe_2$ to 1T $MoSe_2$ [34]. In addition, those peaks at 31.3°, 35.7°, 42.1°,45.8°, 54.8° assigning to the (100), (103), (006), (105), and (110) plane of hexagonal 2H shifts to a lower degree also mean the expansion of interlayer spacing and the transformation of some crystal structures from 2H $MoSe_2$ to 1T $MoSe_2$ phase[35]. The Raman spectrum (Figure 1b) further identify the phase composition of CC/$MoSe_2$. As shown in Figure 1b, two characteristic peaks occur at 236.5 and 282 cm^{-1}, indexing to the phonon modes of 2H phase $MoSe_2$ A_{1g} and E_{2g}, respectively. In addition, there are three peak at 104.1, 149.6, and 221.2 cm^{-1}, corresponding to the J_1, J_2 and J_3 phonon modes of 1T phase $MoSe_2$. Besides, it still appears two peaks at 1360 and 1582 cm^{-1}, which correspond to the D band and G band of disordered carbon in hexagonal graphitic layers and characteristic of defects [36, 37]. The high resolution XPS are confirmed the chemical binding states of composites. For the 3d spectra of Mo (Figure 1c), the binding energies of two peaks located between 227-234 eV represent the Mo $3d_{5/2}$ and Mo $3d_{3/2}$ orbitals. Furthermore, those peaks at 229.1 eV and 232.4 eV are ascribe to the 1T phase $MoSe_2$. The other peaks at 229.9 eV and 230.0 eV are index to the 2H phase $MoSe_2$.The ratio of 1T phase to 2H phase is 7/5 by calculating the area integral, indicating high mixture phase composition. The FESEM image (Figure 1d) further observes that a lot of nanosheets structure closely grown on the carbon cloth with interlaced each other. From the FESEM of surface of CC in Figure 1e, it can observe typical two dimensional structure for those nanosheets. From the HRTEM of Figure 1f, those two dimensional nanosheets display large surface and porous structure, which provides abundant edges. The thickness of those nanosheets are about 3-5 layers (Figure 1g), indicating ultrathin layer structure. The layers spacing

measured from nanosheets range from 0.65 nm to 0.71 nm. It is known that (002) crystal plane of 2H-$MoSe_2$ is 0.65 nm from the PDF card (No. 29-0914) [12]. The little increase of interlayer indicates that partly 1T phase $MoSe_2$ exists in structure, which is consistent with the results of XPS.

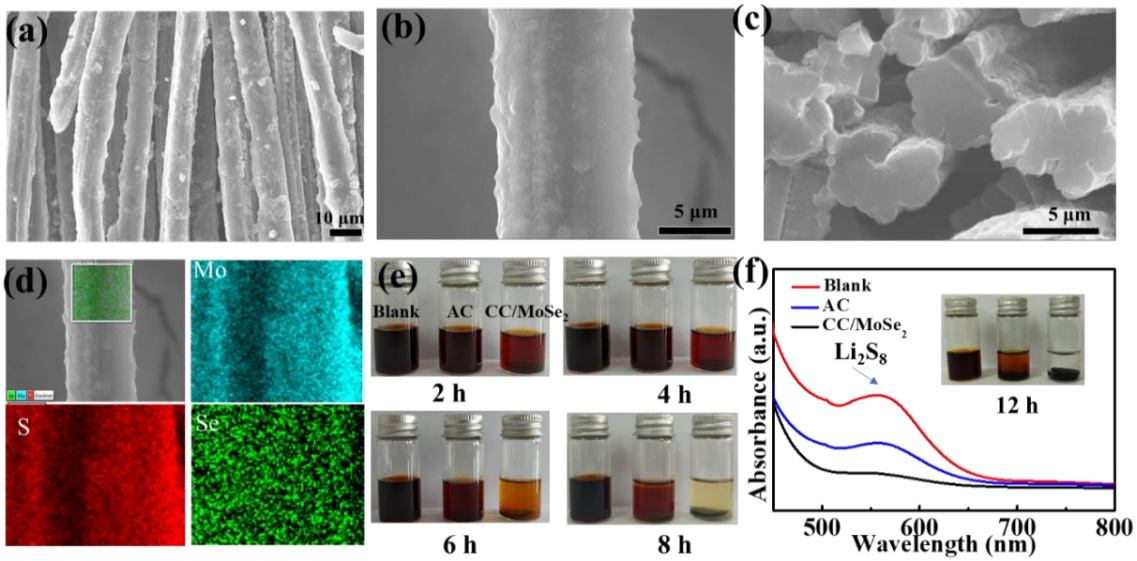

Figure 2. (a-d) SEM images and EDS Mapping of electrochemical reduction of Li_2S_8 on CC/$MoSe_2$; (e) digital photos of AC and CC/$MoSe_2$ immersed in the Li_2S_8 solution after different time, (f) UV−vis spectra and associated color changes of the Li_2S_8 solution exposure to AC and CC/$MoSe_2$ for 12 h.

After in situ Li_2S by liquid reduction of Li_2S_8 catholyte, the morphology and microstructure of the CC/$MoSe_2$ (Figure 2a and 2b) show smooth surface with thickness coating layers without the original $MoSe_2$ structure. It indicates Li_2S has been uniform deposited on the surface of electrode. From the cross-section of CC/$MoSe_2$ fibers can be also confirmed that the outside of fiber surface are fully filled (Figure 2c). SEM and EDS elemental mappings indicate uniform spatial distribution of Mo, S, and Se elements over the detection range of the hybrid electrode composites (Figure 2d). It demonstrates that in situ deposition can facilitate solid Li_2S uniformly distribution on the CC/$MoSe_2$ electrode due to the high uniform $MoSe_2$ nanostructure. The adsorption capability of intermediate LiPSs are further compared by the visible absorption test according to immerse contain 10 mg AC and $MoSe_2$ powders in the 5 mM, 5mL Li_2S_8 catholyte, respectively (Figure 2e). It is apparent that the color of the solution containing $MoSe_2$ powder significantly faded and became almost colorless as compared with the blank solution after 12 h (insert digital photograph). At the same time, the solution containing the activated carbon (AC) changes from dark red brown to light red color, indicating weak adsorption capacity for Li_2S_8. In addition, to more specifically quantify their adsorption capacity, the ultraviolet absorption spectrum are further analyzed the adsorption peak intensity of S_8^{2-} (Figure 2f) [38]. It is worth noting that the characteristic peak of S_8^{2-} at 560 nm becomes weaker after adsorbing by $MoSe_2$. On the contrast, there is significant peak at 560 nm for AC, suggesting limited soluble LiPSs adsorption ability.

Based on above visible experiment, it can be found that CC/$MoSe_2$ electrode shows strong LiPSs adsorption ability as well as high efficient in situ LiPSs deposition capability. The LiPSs conversion

ability are further evaluated by the following electrochemical investigation. Firstly, the CV test of the CC/$MoSe_2$ and AC electrode are carried out at the scan rate of 0.1 mV s^{-1} (Figure 3).

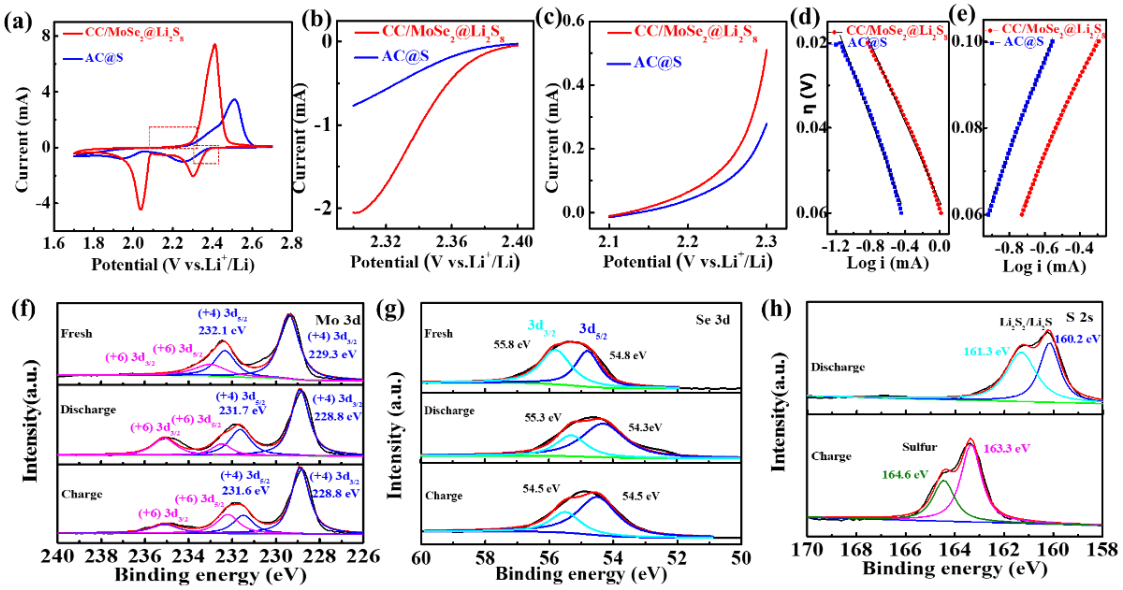

Figure 3. (a) the CV curves of AC and CC/$MoSe_2$ electrode at the first cathodic and anodic process at the scan rate of 0.1mV s^{-1}; the corresponding potentiostatic polarization curves of AC and CC/$MoSe_2$ at the initial (b) cathodic and (c) anodic process; Tafel plots of AC and CC/$MoSe_2$ derived from the potentiostatic polarization curves at (d) cathodic and (e) anodic process; high-resolution XPS spectrum of (f) Mo, (g)Se and (h) S element of CC/$MoSe_2$ at fresh and discharge/charge state, respectively.

Both AC and CC/$MoSe_2$ exhibit two typical cathodic peaks and one anodic peak. Those two cathodic peaks are assigned to the S_8^- convert into dissolved LiPSs and nucleation of Li_2S. The two cathodic peak intensities for AC are much smaller than those of CC/$MoSe_2$, indicating higher LiPSs conversion and nucleation kinetics. The higher conversion efficiency of LiPSs for CC/$MoSe_2$ will largely increase the Li_2S electrochemical activity, and result in much stronger oxidation reaction of Li_2S_x ($4 \leq x \leq 8$, 2.3 V-2.5 V) [39, 40]. In addition, the CC/$MoSe_2$ electrode has a smaller potential difference between the oxidation peak potential and the minimum reduction peak, indicating smaller polarization during the phase conversion [23]. The potentiostatic polarization curves interception from the dashed range of Figure 3a for both cathodic sweep and anodic sweep (Figure 3b) are further estimate LiPSs redox kinetics. The peak current for the potentiostatic polarization curves of Figure 3b corresponds to the beginning conversion from Li_2S_8 to Li_2S_6/Li_2S_4. The CC/$MoSe_2$ electrode displays larger current increase but lower polarization overpotential, indicating more sufficient long chain LiPSs converted to short chain LiPSs capability. Further maintain higher nucleation of deposited of Li_2S on the electrode. Except for the stronger reduction process, for the oxidation process at 2.1 V (Figure 3c), the CC/$MoSe_2$ also shows higher oxidation peak, confirming that the decomposition of Li_2S on CC/$MoSe_2$ electrode is much faster than AC electrode. Furthermore, the relationship of overpotential (η) vs. log(i) of the two different electrodes derived from potentiostatic polarization curves are displayed in Figure 3d and 3e. According to the Tafel equation ($\eta = a + b*\log(i)$) to calculated the exchange current density (i), the

reduction/oxidation i values are 0.680/0.273 mA cm^{-2} for CC/$MoSe_2$ electrode, while AC displays much smaller i values of 0.042/0.029 mA cm^{-2-}, respectively. Thus, it means the CC/$MoSe_2$ electrode has faster electronic transfer kinetics during the reversible LiPSs conversion process, which can accelerate the LiPSs quickly nucleation and converting to Li_2S on the electrode. Thus, the regulation of nucleation Li_2S on CC/$MoSe_2$ electrode can not only alleviate the agglomeration of Li_2S, but also largely increase Li_2S redox electrochemical activity [41, 42].

The strong interaction between S/Li_2S on CC/$MoSe_2$ are confirmed by the XPS spectra before and after cycling. As shown in the Mo high-resolution XPS spectrum (Figure 3f) for CC/$MoSe_2$ electrode, there are two peaks appear at 229.3 and 223.1 eV, which index to the Mo^{4+} 3d $_{3/2}$ and Mo^{4+} 3d $_{5/2}$, respectively. However, at the discharge and charge states, both Mo^{4+} 3d $_{3/2}$ and Mo^{4+} 3d $_{5/2}$ shift to lower binding energy. In addition, at fully discharge state, a new peak appears at 235.0 eV, which is ascribe to the Mo^{6+} binding energy for CC/$MoSe_2$, implying Mo^{4+} are partly oxidized into higher valent value. It indicates that there is electron transfer from $MoSe_2$ to LiPSs during discharge process. When return to charge, the peak intensity of Mo^{6+} becomes weaken again, suggesting high valent state Mo^{6+} are reduction along with the conversion of LiPSs to sulfur.

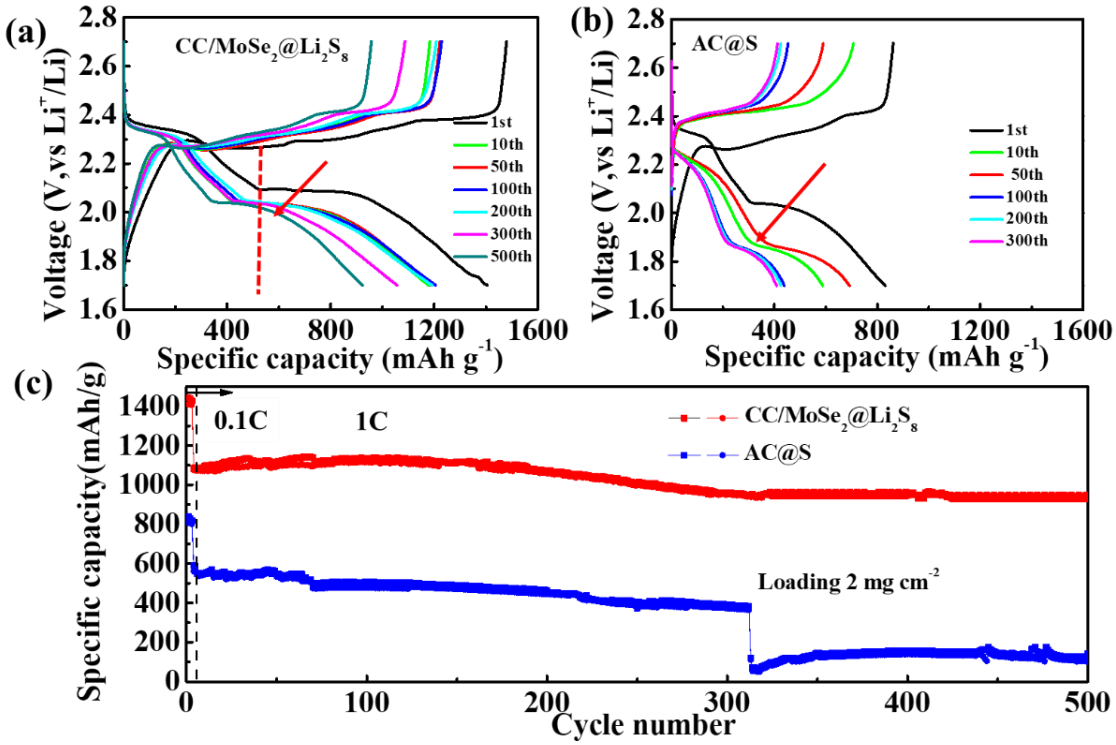

Figure 4. The galvanostatic discharge–charge curves of (a) CC/$MoSe_2$@Li_2S_8 and (b) AC@S at 1C; (c) the cycling performance of CC/$MoSe_2$@Li_2S_8 and AC@S at 1C with sulfur loading of 2.0 mg cm^{-2} with E/S ratio of 12.5.

Those phenomenon directly demonstrates a strong chemical binding interaction between deposition products and $MoSe_2$ [34]. Meanwhile, for the high-resolution XPS spectrum of Se (Figure 3g), two peaks appear at 54.8 and 55.8 eV for fresh CC/$MoSe_2$, ascribing to the Se 3d $_{3/2}$ and 3d $_{5/2}$,

respectively. At the discharge and charge states, both Se 3d $_{3/2}$ and 3d $_{5/2}$ shift to lower binding energy, which shows electronic density around Se also change during the LiPSs conversion process. Furthermore, Figure 3h shows the S 2s spectrum for CC/$MoSe_2$ electrode in the discharged and charged state. At the fully discharge state, there is strong peak appears between 158-164 eV, which assign to the Li_2S_2(160.2 eV) and Li_2S (161.3 eV) binding energies. The absence of sulfur peak after discharge indicates LiPSs are fully converted on the CC/$MoSe_2$ electrode. In addition, the XPS spectrum of S 2s at the charged state also only shows typical sulfur peaks at 163.3 and 164.6 eV, implying high reversible Li_2S/S redox capability on the CC/$MoSe_2$ electrode. The strong electrochemical reactive kinetics are responsible for the rich edge sites, providing high electrocatalytic activity [23, 43]. Figure 4a and 4b show the galvanostatic charge-discharge profiles of AC@S and CC/$MoSe_2$@Li_2S_8 electrode at a current density of 1C (1C =1675 mAh g^{-1}). There are two discharge plateaus along with one charge plateau for both AC@S and CC/$MoSe_2$@Li_2S_8. However, for the discharge process of CC/$MoSe_2$@Li_2S_8, there is a much longer high potential plateaus from 2.4 V to 2.07 V, which has higher capacity contribution for the initial discharge process.

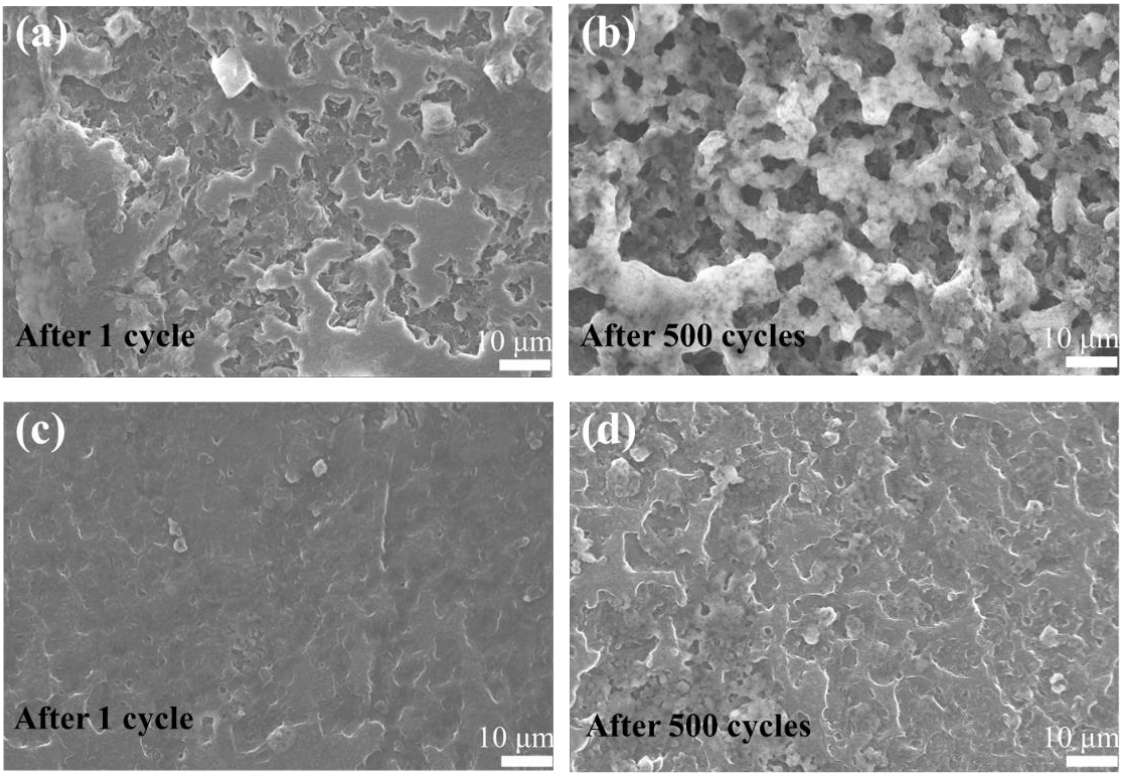

Figure 5. (a) and (b) SEM images of counter Li metal anode for AC cathode after first cycle, 500 cycles, respectively; (c) and (d) SEM images of counter Li metal anode for CC/$MoSe_2$ cathode first cycle, 500 cycles, respectively.

This discharge stage is related with the LiPSs continuing conversation before the nucleation of Li_2S [41, 44]. It confirms that CC/$MoSe_2$ electrode largely increase the conversion activity of soluble Li_2S_8. Thus, further reduction process also displays much longer voltage platform at 2.07 V, which reflects higher nucleation and growth capability of Li_2S for CC/$MoSe_2$@Li_2S_8 electrode. At the

subsequent long cycling, the CC/$MoSe_2$@Li_2S_8 electrode exhibits much smaller voltage polarization than comparing with AC@S electrode. The long cycling performance of those two electrodes are further compared. When under the sulfur loading of 2 mg cm^{-2} at E/S ratio of 12.5 μL mg^{-1} (Figure 4c), it displays a high initial charge capacity of 1441 mAh g^{-1} at the first cycle at 0.1C for CC/$MoSe_2$@Li_2S_8 electrode, which is near to the theoretical capacity of sulfur. The high initial discharge capacity implies that the solid Li_2S completely depositing on the CC/$MoSe_2$ electrode. Then, it exhibits 1142 mAh g^{-1} charge capacity at 1C and still remains stable capacity at 927 mAh g^{-1} after 500 cycles with 81.2% capacity retentions. For comparison, at the beginning for AC@S electrode, although it displays capacity of 839 mAh g^{-1} at the initial charge process, it only delivers low capacity of 567 mAh g^{-1} at 1C. The low initial capacity reflects that sluggish sulfur redox kinetics on AC@S electrode. In addition, it quickly decreases from 365 mAh g^{-1} to 110 mAh g^{-1} after 313 cycles at 1C. The suddenly deteriorate of electrochemical stability might cause by gradually exhausting of electrolyte due to the formation of unstable SEI layer on the lithium anode side due to the deteriorative LiPSs shuttle effort, which hinder the Li metal redox reaction [45]. This phenomenon can be confirmed by the following discussion. From the FESEM of counter lithium metal for AC@S electrode after 1st and 500th cycles (Figure 5a and 5b), it displays rough and porous surface. It means lithium metal suffering from continuous chemical reaction with LiPSs. However, for counter lithium anode of CC/$MoSe_2$@Li_2S_8 electrode, even after 500 cycles (Figure 5d), the corresponding FESEM image of lithium anode appears uniform and dense morphology without obvious passivation layer comparing with the initial cycles (Figure 5c). This implies that CC/$MoSe_2$ electrode has strong conversion ability of LiPSs, which largely alleviate the shuttle efforts of LiPSs, resulting the less side reaction on counter lithium metal anode.

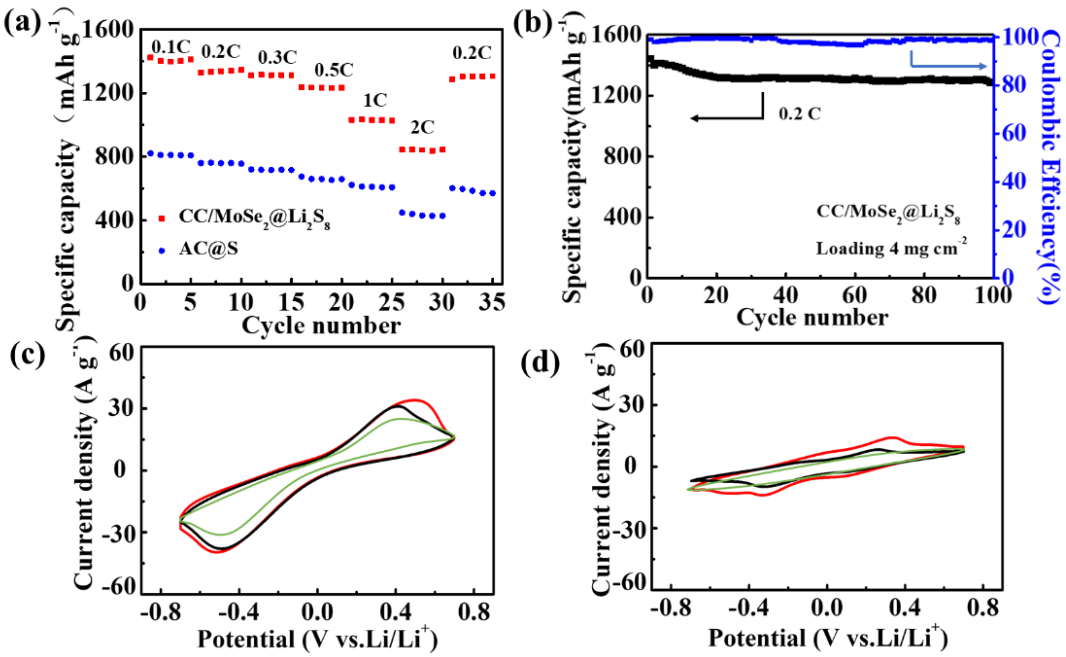

Figure 6. (a) the rate capability of CC/$MoSe_2$@Li_2S_8 and AC@S; (b) the cycling performance of CC/$MoSe_2$ at 0.2C with higher sulfur loading of 4 mg cm^{-2} with E/S ratio of 6.2; CV curve of (c) CC/$MoSe_2$||LiPSs||CC/$MoSe_2$ and (d) AC||LiPSs||AC symmetrical cells at the voltage window of -0.7 to 0.7V, respectively.

The rate performance of AC@S and CC/$MoSe_2$@Li_2S_8 electrode are further compared as shown in Figure 6a. Obviously, CC/$MoSe_2$@Li_2S_8 electrode obtains much higher discharge capacities, delivering 1441, 1405, 1371, 1264, 1065, 872 mAh g^{-1} at 0.1, 0.2, 0.3, 0.5, 1, and 2C, respectively. When the current density returned to 0.2C, it can restore to 1386 mAh g^{-1}, indicating that $MoSe_2$ provides fast electron transfer kinetics to facilitate the LiPSs conversion. However, AC@S electrode only achieves poor rate performance, especially at high rate at 2C, it only obtains 432 mAh g^{-1}, demonstrating sluggish LiPSs redox kinetics. When the rate returns to 0.2C, it still has a rapid capacity decay during cycling, which means some sulfur lost electrochemical activity. The strong contrast evidence that CC/$MoSe_2$@Li_2S_8 electrode has higher charge transport ability of LiPSs, resulting from the high electrocatalytic activity of $MoSe_2$. The powerful charge transport ability of CC/$MoSe_2$ electrode not only accelerates the solid/liquid phase conversion LiPSs, but also alleviates the soluble LiPSs migration between cathode and anode, so as to maintain high sulfur electrochemical activity. Even at higher sulfur loading (4.0 mg cm^{-2}) at extreme low E/S ratio of 6.25 μL mg^{-1}, the CC/$MoSe_2$@Li_2S_8 electrode still obtains high initial capacity of 1386 mAh g^{-1} at 0.2C and 93.4% capacity retention after 100 cycles (Figure 6b), which is comparable with the state-of-art host sulfur cathodes materials listed in Table 1.

Table 1. The comparison of CC/$MoSe_2$ with other host cathode materials in Li-S battery

Materials	Sulfur loading (mg cm^{-2})	E/S (μL mg^{-1})	Electrochemical performance	Ref.
CC/$MoSe_2$@Li_2S_8	2	12.5	1 C, 927 mAh g^{-1}, 500 cycles	This work
	4	6.25	0.2 C, 1204 mAh g^{-1}, 100 cycles	
PCF/VN/S	8	20	0.1C, 1052 mAh g^{-1}, 250 cycles	[46]
CNF sheets/S	2.4	33	1/3 C, 683 mAh g^{-1}, 500 cycles	[47]
rGO/S	1.0	35	0.1 A g^{-1} , 889 mAh g^{-1}, 200 cycles	[48]
MWCNTs/S	3.2	28	0.1C, 760 mAh g^{-1}, 160 cycles	[49]
TiN-VN/S	1.5	16	1C, 700 mAh g^{-1}, 800 cycles	[42]
VO_2(P)-NCNT/S	4.8	20.8	1C, 804 mAh g^{-1}, 500 cycles	[41]
Co_9S_{8-x}/CNT/S	2	20	0.3C, 648 mAh g^{-1}, 1000 cycles	[50]
CC@CoP/C/S	4.17	30	2C, 833 mAh g^{-1}, 600 cycles	[51]
MoN-VN/S	3	15	2C, 708 mAh g^{-1}, 500 cycles	[52]
CoS_2/G/S	0.4	30	0.5C, 1000 mAh g^{-1},250 cycles	[53]

The excellent electrochemical performance are strong related with the intermediate LiPSs conversation kinetics, which can be identified by assembly of asymmetrical cells using Li_2S_6 electrolyte in AC and CC/$MoSe_2$ electrode. As shown in Figure 6c, the CV curves of CC/$MoSe_2$ electrode appear stronger current peaks under scan rates from 10 to 50 mV s^{-1}, indicating that LiPSs redox activity significantly increase comparing with AC (Figure 6d). Meanwhile, the appearance of high symmetry at every scan rates for the reduction/oxidation peaks of CC/$MoSe_2$ electrode also demonstrates CC/$MoSe_2$ can function as bi-catalysis toward $Li_2S \leftrightarrow Li_2S_6 \leftrightarrow S$ mutual transformation.

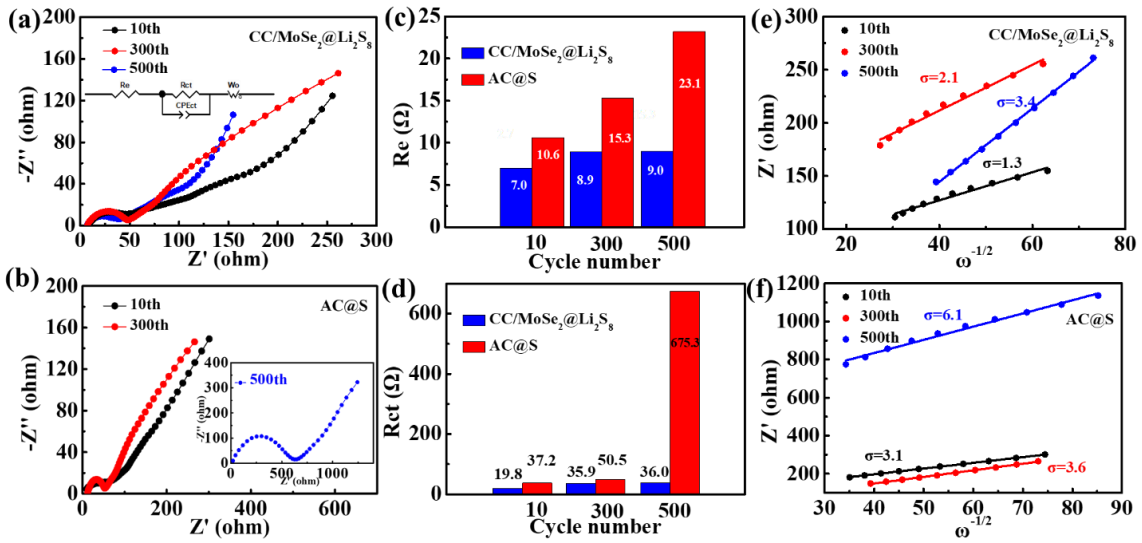

Figure 7. (a) and (b) the Nyquist plots of CC/$MoSe_2$@Li_2S_8 and AC@S electrodes cycle at 10th, 300th, 500th, respectively; (c) R_e and (d) R_{ct} of CC/MoS_2 and CC electrodes cycle at 10th, 300th, 500th, respectively; resistance of Z` vs.$\omega^{-1/2}$ after different cycle for (e) CC/$MoSe_2$ and (f) AC electrodes.

The Li ion diffusion kinetics and resistance change of CC/$MoSe_2$@Li_2S_8 and AC@S electrode are evaluated by EIS measurement. As shown in Figure 7a and 7b, the Nyquist plots of both AC@S and CC/$MoSe_2$@Li_2S_8 electrodes after different cycles are composed of a semicircle along with an inclined line, which can be fitted by the equivalent circuit of inset Figure 7a. The intercept on the real axis at high frequency are related to the interface resistance (R_E) of the electrolyte and electrode. The diameter of the semicircle index to the charge transfer resistance (R_{CT}) [54, 55]. The R_E and R_{CT} are compared in Figure 7c and 7d. Based on the fitting curves, the R_E of CC/$MoSe_2$@Li_2S_8 electrode after 10 cycles (7.0 Ω) is smaller than AC@S electrode (10.6 Ω). It is attributed to the abundant $MoSe_2$ edges, providing amount active sites to improve the uniform nucleation of charge/discharge products (S/Li_2S) at the surface of CC/$MoSe_2$ electrode. After 500 cycles, the R_E of CC/$MoSe_2$@Li_2S_8 electrode only increases to 9 Ω, while AC@S electrode largely increase to 23.1 Ω, which means a lot of electrolytes are consumed on AC electrode. Meanwhile, comparing the R_{CT} for the two electrodes, it is important to note that the R_{CT} of AC@S electrode dramatically increased from 37.2 Ω at 10^{th} to 675.3 Ω at 500^{th} cycles. The significant resistance increase implies larger hindering of charge transfer on AC@S electrode, might result in decrease of sulfur electrochemical activity. The phenomenon is consistent with the suddenly decay of

the capacity for AC@S electrode after 313 cycles (Figure 4c). The suddenly decrease of charge transfer capability is attributed to the shuttle effort of LiPSs along with consumption of electrolyte after long cycling, resulting in the formation of "dead sulfur". On the contrast, the R_{CT} of CC/$MoSe_2$@Li_2S_8 exhibits smaller resistance change even after 500 cycles. This demonstrates that the CC/$MoSe_2$ contribute to stable electrode interface to enhance the redox kinetics of LiPSs during cycling. Then, the Li-ion diffusion coefficient of the two electrodes are calculated as the following equation [56, 57].

$$D=R^2T^2/2A^2n^4F^4c^2\sigma_w^2 \quad \text{(Eq.1)}$$

Where D is Li-ion diffusion coefficient, R is the gas constant, T is the absolute temperature, A is the electrode area, n is the number of electrons transferred per molecule during electrochemical reaction, F is Faraday constant, σ_w is the Warburg impedance coefficient, and c is molar concentration of Li^+.

Table 2. Comparison of D_{Li^+} (Li ion diffusion coefficient) of AC and CC/$MoSe_2$ electrode after different cycle.

D_{Li^+} ($cm^2\ s^{-1}$)	After 10 cycles	After 300 cycles	After 500 cycles
AC@S	9.7×10^{-11}	7.2×10^{-11}	2.8×10^{-12}
CC/$MoSe_2$@Li_2S_8	5.5×10^{-10}	1.9×10^{-10}	8.1×10^{-11}

The Li ion diffusion coefficients (Table 2) for CC/$MoSe_2$@Li_2S_8 are 5.5×10^{-10} $cm^2\ s^{-1}$,1.9×10^{-10} $cm^2\ s^{-1}$ and 8.1×10^{-11} $cm^2\ s^{-1}$, at 10^{th}, 300^{th} and 500^{th} cycle. Although the Li ion diffusions coefficient after 500^{th} cycles has a little decrease, it still has one order of magnitude higher than that of AC@S electrode (2.8×10^{-12} $cm^2\ s^{-1}$). The relatively higher Li-ion diffusion coefficient confirm that the stronger lithium ion diffusion kinetics on CC/$MoSe_2$ electrode.

Based on the above discussion, the binder free CC/$MoSe_2$ electrode displays high Li_2S_8 chemical adsorption and conversion kinetics at the beginning of deposition process due to their abundant electrocatalytic active sites, regulating uniform nucleation and growing Li_2S on CC/$MoSe_2$ electrode. The in situ catalytic and electrochemical deposition would accelerate the solid/liquid/solid phase conversion process between S_8/LiPSs/Li_2S, causing less LiPSs shuttle efforts and improving sulfur electrochemical activity. Thus, even at the low E/S environment, the CC/$MoSe_2$ still presents high charge transform ability to facilitate the transformation of LiPSs. The dynamic regulation of Li_2S nucleation/growth at the early reaction stage provides more opportunity for uniform deposition of active materials so as to guarantee the subsequent high sulfur utilization.

4. CONCLUSION

In summary, flexible binder free electrode consisting of 2D few-layered $MoSe_2$ nanosheets growing on carbon cloth are rationally designed and prepared by one step hydrothermal method. Through the systematic investigations, the superiorities of CC/$MoSe_2$ electrode as the sulfur host matrix are

unveiled in detail. Take advantage of the high electrocatalytic activity from the unique CC/$MoSe_2$ nanostructure, it largely accelerates the conversion intermediate LiPSs and further dynamic regulates the nucleation and growth of Li_2S according to utilization Li_2S_8 as active materials. Thus, Li_2S can be uniform deposited on CC/$MoSe_2$ electrode and maintains high redox kinetics on electrodes. These merits make CC/$MoSe_2$@Li_2S_8 contribute to excellent electrochemical performance at low E/S environment in Li-S battery. Therefore, such flexible metal selenide self-standing electrodes are considered as promising electrocatalytic host matrix for solving the sluggish of LiPSs conversion and enhancing the utilization of sulfur toward flexible electronic devices and large-scale energy storage equipment in Li-S battery.

ACKNOWLEDGMENTS
We acknowledge the National Natural Science Foundation of China (grant No. 51502250, 51604250), the Science & Technology Department of Sichuan Province (grant no. 2019YFG0220, 2017JQ0044, 2019-GH02-00052-HZ), Youth Science and Technology Innovation Team of Energy Material Electrochemistry of Southwest Petroleum University (grant No.2015CXTD04), and Key Project of Extracurricular Open Fund of Southwest Petroleum University (KSZ18520).

References

1. S. Chu, Y. Cui, N. Liu, *Nat. Mater.,* 16 (2016) 16-22.
2. R. Xu, I. Belharouak, X. Zhang, R. Chamoun, C. Yu, Y. Ren, A. Nie, R. Shahbazian-Yassar, J. Lu, J.C.M. Li and K. Amine, *ACS Appl. Mater. Interfaces*, 6 (2014) 21938-21945.
3. X. Ji, K.T. Lee and L.F. Nazar, *Nat. Mater.,* 8 (2009) 500-506.
4. D. Larcher and J.M. Tarascon, *Nat. Chem.,* 7 (2014) 19-29.
5. M.-S. Wang, G.-L. Wang, S. Wang, J. Zhang, J. Wang, W. Zhong, F. Tang, Z.-L. Yang, J. Zheng and X. Li, *Chem. Eng. J.*, 356 (2019) 895-903.
6. G. Zhou, S. Pei, L. Li, D.-W. Wang, S. Wang, K. Huang, L.-C. Yin, F. Li and H.-M. Cheng, *Adv. Mater.,* 26 (2014) 625-631.
7. Z. Lin and C. Liang, *J. Mater. Chem. A*, 3 (2015) 936-958.
8. Q. Pang, C.Y. Kwok, D. Kundu, X. Liang and L.F. Nazar, *Joule*, 3 (2019) 136-148.
9. X. Liang, C. Hart, Q. Pang, A. Garsuch, T. Weiss and L.F. Nazar, *Nat. Commun.,* 6 (2015) 5682.
10. A. Manthiram, S.-H. Chung and C. Zu, *Adv. Mater.,* 27 (2015) 1980-2006.
11. Z.W. Seh, Y. Sun, Q. Zhang and Y. Cui, *Chem. Soc. Rev.,* 45 (2016) 5605-5634.
12. H. Wong, X. Ou, M. Zhuang, Z. Liu, M.D. Hossain, Y. Cai, H. Liu, H. Lee, C.-Z. Wang and Z. Luo, *ACS Appl. Mater. Interfaces,* 11 (2019) 19986-19993.
13. H. Yuan, H.-J. Peng, B.-Q. Li, J. Xie, L. Kong, M. Zhao, X. Chen, J.-Q. Huang and Q. Zhang, *Adv. Energy Mater.*, 9 (2019) 1802768.
14. Q. Lu, Q. Zhu, W. Guo and X. Li, *Ionics,* 25 (2019) 3107-3119.
15. Y. Wang, X. Huang, S. Zhang and Y. Hou, *Small Methods,* 2 (2018) 1700345.
16. T. Tang and Y. Hou, *Electro. Ener. Rev.*, 1 (2018) 403-432.
17. Y. Yi, H. An, P. Zhang, X. Tian, P. Yang, P. Liu, T. Wang, L. Qu, M. Li, G. Yang and B. Yang, *Chem. Nano Mat.*, 5 (2019) 926-931.
18. Z. Wei Seh, W. Li, J.J. Cha, G. Zheng, Y. Yang, M.T. McDowell, P.C. Hsu and Y. Cui, *Nat. Commun.*, 4 (2013) 1331.
19. J. Zhang, Y. Shi, Y. Ding, W. Zhang and G. Yu, *Nano Lett.*, 16 (2016) 7276-7281.
20. P. Cheng, K. Sun and Y.H. Hu, *RSC Adv.*, 6 (2016) 65691-65697.
21. J.D. Shen, X.J. Xu, J. Liu, Z.B. Liu, F.K. Li, R.Z. Hu, J.W. Liu, X.H. Hou, Y.Z. Feng, Y. Yu and M. Zhu, *ACS Nano,* 13 (2019) 8986-8996.

22. G.X. Liu, K. Feng, H.T. Cui, J. Li, Y.Y. Liu and M.R. Wang, *Chem. Eng. J.*, 381 (2020) 9.
23. J. Park, B.-C. Yu, J.S. Park, J.W. Choi, C. Kim, Y.-E. Sung and J.B. Goodenough, *Adv. Energy Mater.*, 7 (2017) 1602567.
24. L. Zhang, D. Sun, J. Kang, J. Feng, H.A. Bechtel, L.-W. Wang, E.J. Cairns and J. Guo, *Nano Lett.*, 18 (2018) 1466-1475.
25. Z. Yuan, H.J. Peng, T.Z. Hou, J.Q. Huang, C.M. Chen, D.W. Wang, X.B. Cheng, F. Wei and Q. Zhang, *Nano Lett.*, 16 (2016) 519-527.
26. T.Q. Zhang, H.X. Wang and J.X. Zhao, *New J. Chem.*, 43 (2019) 9396-9402.
27. X.C. Dai, M.H. Huang, Y.B. Li, T. Li, B.B. Zhang, Y.H. He, G.C. Xiao and F.X. Xiao, *J. Mater. Chem. A*, 7 (2019) 2741-2753.
28. X.L. Yin, L.L. Li, M.L. Liu, D.C. Li, L. Shang and J.M. Dou, *Chem. Eng. J.*, 370 (2019) 305-313.
29. J.H. Lin, P.C. Wang, H.H. Wang, C. Li, X.Q. Si, J.L. Qi, J. Cao, Z.X. Zhong, W.D. Fei and J.C. Feng, *Adv. Sci.*, 6 (2019) 14.
30. Y.N. Guo, T. Park, J.W. Yi, J. Henzie, J. Kim, Z.L. Wang, B. Jiang, Y. Bando, Y. Sugahara, J. Tang and Y. Yamauchi, *Adv. Mater.*, 31 (2019) 34.
31. Y.K. Liu, S. Jiang, S.J. Li, L. Zhou, Z.H. Li, J.M. Li and M.F. Shao, *Appl. Catal. B-Environ.*, 247 (2019) 107-114.
32. J. Yi, H. Li, Y. Gong, X. She, Y. Song, Y. Xu, J. Deng, S. Yuan, H. Xu and H. Li, *Appl. Catal. B-Environ.*, 243(2019) 330-336.
33. D. Vikraman, S. Hussain, K. Karuppasamy, A. Feroze, A. Kathalingam, A. Sanmugam, S.-H. Chun, J. Jung and H.-S. Kim, *Appl. Catal. B-Environ.*, 264 (2020) 118531.
34. C.-Y. Fan, Y.-P. Zheng, X.-H. Zhang, Y.-H. Shi, S.-Y. Liu, H.-C. Wang, X.-L. Wu, H.-Z. Sun and J.-P. Zhang, *Adv. Energy Mater.*, 8 (2018) 1703638.
35. W. Xiao, D. Bukhvalov, Z. Zou, L. Zhang, Z. Lin and X. Yang, *ChemSusChem*, 12 (2019) 5015-5022.
36. C. Yu, Z. Cao, S. Chen, S. Wang and H. Zhong, *Appl. Surf. Sci.*, 509 (2020) 145364.
37. S. Deng, C. Ai, M. Luo, B. Liu, Y. Zhang, Y. Li, S. Lin, G. Pan, Q. Xiong, Q. Liu, X. Wang, X. Xia and J. Tu, *Small*, 15 (2019) e1901796.
38. S.H. Chung and A. Manthiram, *Adv. Energy Mater.*, 9 (2019) 1901397.
39. M. Chen, W. Xu, S. Jamil, S. Jiang, C. Huang, X. Wang, Y. Wang, H. Shu, K. Xiang and P. Zeng, *Small*, 14 (2018) 1803134.
40. Y. Wei, Z. Kong, Y. Pan, Y. Cao, D. Long, J. Wang, W. Qiao and L. Ling, *J. Mater. Chem. A*, 6 (2018) 5899-5909.
41. S. Wang, J. Liao, X. Yang, J. Liang, Q. Sun, J. Liang, F. Zhao, A. Koo, F. Kong, Y. Yao, X. Gao, M. Wu, S.-Z. Yang, R. Li and X. Sun, *Nano Energy*, 57 (2019) 230-240.
42. Z. Xing, G. Li, S. Sy and Z. Chen, *Nano Energy*, 54 (2018) 1-9.
43. X.-Q. Zhang, X. Chen, L.-P. Hou, B.-Q. Li, X.-B. Cheng, J.-Q. Huang and Q. Zhang, *ACS Energy Lett.*, 4 (2019) 411-416.
44. G. Babu, N. Masurkar, H. Al Salem and L.M. Arava, *J. Am. Chem. Soc.*, 139 (2017) 171-178.
45. X. Chen, T. Hou, K.A. Persson and Q. Zhang, *Mater. Today*, 22 (2019) 142-158.
46. Y. Zhong, D. Chao, S. Deng, J. Zhan, R. Fang, Y. Xia, Y. Wang, X. Wang, X. Xia and J. Tu, *Adv. Funct. Mater.*, 28 (2018) 1706391.
47. L. Qie, C. Zu and A. Manthiram, *Adv. Energy Mater.*, 6 (2016) 1502459.
48. C. Wang, X. Wang, Y. Wang, J. Chen, H. Zhou and Y. Huang, *Nano Energy*, 11 (2015) 678-686.
49. S.R. Thieme, J. Brückner, I. Bauer, M. Oschatz, L. Borchardt, H. Althues and S. Kaskel, *J. Mater. Chem. A*, 1 (2013) 9225.
50. H. Lin, S. Zhang, T. Zhang, S. Cao, H. Ye, Q. Yao, G.W. Zheng and J.Y. Lee, *ACS Nano*, 13 (2019) 7073-7082.
51. Z. Wang, J. Shen, J. Liu, X. Xu, Z. Liu, R. Hu, L. Yang, Y. Feng, J. Liu, Z. Shi, L. Ouyang, Y. Yu and M. Zhu, *Adv. Mater.*, 31 (2019) e1902228.

52. C. Ye, Y. Jiao, H. Jin, A.D. Slattery, K. Davey, H. Wang and S.Z. Qiao, *Angew Chem. Int. Ed.,* 57 (2018) 16703-16707.
53. Z. Yuan, H.-J. Peng, T.-Z. Hou, J.-Q. Huang, C.-M. Chen, D.-W. Wang, X.-B. Cheng, F. Wei and Q. Zhang, *Nano Lett.,* 16 (2016) 519-527.
54. M.-S. Wang, Z.-Q. Wang, Z. Chen, Z.-L. Yang, Z.-L. Tang, H.-Y. Luo, Y. Huang, X. Li and W. Xu, *Chem. Eng. J.*, 334 (2018) 162-171.
55. X. Li, K. Zhang, D. Mitlin, Z. Yang, M. Wang, Y. Tang, F. Jiang, Y. Du and J. Zheng, *Chem. Mater.,* 2018, 30, 2566-2573.
56. X. Li, K. Zhang, M. Wang, Y. Liu, M. Qu, W. Zhao and J. Zheng, *Sustainable Energy Fuels.*, 2018, 2, 413-421.
57. R. Zhang, M. Wu, X. Fan, H. Jiang and T. Zhao, *J. Power Sources*, 436 (2019) 226840.